Anatomy of a solar flare: Part I. The solar quake measurements of the December 14, 2006 X-class flare with GONG, Hinode and RHESSI

S.A. Matthews[1], S. Zharkov[1], V.V.Zharkova[2]

ABSTRACT

Some of the most challenging observations to explain in the context of existing flare models are those related to the lower atmosphere and below the solar surface. Such observations, including changes in the photospheric magnetic field and seismic emission, indicate the poorly understood connections between energy release in the corona and its impact in the photosphere and the solar interior. Using data from Hinode, TRACE, RHESSI and GONG we study the temporal and spatial evolution of the 14 December 2006 X-class flare in the chromosphere, photosphere and the solar interior. We report for the first time the detection of a solar quake using time-distance methods applied to GONG data. We then investigate the connections between the emission at various atmospheric depths, with an emphasis on determining the origin of the acoustic responses observed with the GONG data. We report the horizontal displacements observed in the photosphere linked to the timing and locations of the solar quakes associated with this flare, their vertical and horizontal displacement velocities at different atmospheric depths and their implications for models developed for the interpretation of these observations reported in Part II.

Subject headings: Solar: photosphere — helioseismology: acoustic oscillations

1. Introduction

During the last decade it has become well established that flares can and do impact the solar interior, as first predicted by Wolff (1972). The first observations of a 'sun-quake' were reported by Kosovichev & Zharkova (1998) during the flare of 9 July 1996, which

[1]UCL Mullard Space Science Laboratory, University College London, Holmbury St. Mary, Dorking, RH5 6NT UK

[2]University of Bradford, Bradford, UK

reaffirmed the foundations of local helioseismology and provided an additional stimulus for developing its methods further. Since that first identification by time-distance methods, the development of helioseismic holography has led to the identification of many more seismic sources during flares of GOES-class M and X (e.g. Donea et al. 2006; Zharkova & Zharkov 2007; Martínez-Oliveros et al. 2008b). Solar quake observations provide us with unique opportunities to study the excitation of solar oscillations in detail, and raise new questions about the underlying physical processes as well as the properties of the excited waves and sources producing them.

Similarly, confirmation that the photospheric magnetic field routinely changes during flares, both on short timescales (i.e. the duration of the impulsive phase) and longer timescales of hours (before and after a flare) has also become evident in the last decade through the studies by Kosovichev & Zharkova (2001) and Zharkova et al. (2005); Sudol & Harvey (2005, and references therein). Both solar quakes and transient magnetic changes occur during the flare impulsive phase, and thus appear closely related to the initial energy release, and the appearance of enhanced continuum (WL) and hard X-ray (HXR) emission. More long-term magnetic changes (timescales of hours) similarly appear to begin during the impulsive phase and to have a good spatial relationship with WL and HXR emission. This has led to much discussion of the origins of quakes and magnetic changes in the context of the thick target model.

The primary explanations for the origin of acoustic emission during flares have been well summarized by Lindsey & Donea (2008) and Zharkova (2008) and include: chromospheric shocks, which arise as the result of the pressure transients driven by the hydrodynamic response of the ambient plasma to the precipitation of energetic particles (electrons or protons) into the chromosphere (e.g. Kosovichev & Zharkova 1995, 1998; Kosovichev 2006; Zharkova & Zharkov 2007; Donea & Lindsey 2005); pressure transients that are related to backwarming of the photosphere by enhanced chromospheric radiation; (e.g. Lindsey & Braun 2000; Donea et al. 1999; Donea & Lindsey 2005) the Lorentz force transients that occur as a result of the coronal restructuring of the magnetic field (e.g. Zharkova & Kosovichev 2002; Hudson et al. 2008) and the precipitation of particle beams, which themselves carry a strong electric field (Zharkova & Gordovskyy 2006) that in turn induces an electro-magnetic field in the ambient plasma (van den Oord 1990) which modifies the magnetic field of the loop where particles precipitate.

The shocks formed by the hydrodynamic response of the ambient plasma to the precipitation of electron or proton beams seem to be good candidates for the formation of seismic ridges associated with solar flares since they carry sufficient mass and velocity, and thus momentum, to be deposited to the solar photosphere (Kosovichev & Zharkova 1998; Zharkova

& Zharkov 2007). But the question still remains open as to how exactly these shocks deposit their energy into the solar interior (e.g. depths, timescale) and how they can be accounted for from a detailed comparison with seismic observations. These are closely related to the other implications of particle precipitation into a flaring loop, like formation of magnetic transients and non-thermal plasma ionization (Zharkova 2008).

In the case of magnetic changes Lindsey & Donea (2008) highlight that it is the transient component of magnetic changes that is the most relevant to acoustic emission, i.e. those changes that occur on a time-scale of $\tau \approx 2H/c$ or less, where H is the density scale height and c is the sound speed. In the photosphere this timescale is of the order of 40s. The question of whether these short-term transient changes during the impulsive phase can be considered to represent a genuine change in the photospheric magnetic field is still a matter for debate, and the localized sign reversals, or 'magnetic anomalies' (e.g. Qiu et al. 2002) are most often attributed to changes in the line profile occurring as the result of the sudden heating of the ambient plasma or by direct bombardment by high energy particles. In the case of the Ni 6768 Å line used by both GONG and MDI to make magnetic measurements, non-LTE simulations have shown that sudden heating is insufficient to turn this line into emission and that a large increase in electron density is required, i.e. intense particle bombardment (Zharkova & Kosovichev 2002). Observations by Qiu & Gary (2003) that find a good correspondence between the HXR sources and magnetic anomalies lend support to the hypothesis that magnetic field changes are associated with energetic particles. However, simulations of GONG and MDI observations by Edelman et al. (2004) also conclude that magnetic measurements are less sensitive to the changes in the line profile than Doppler measurements.

Recently, Martínez-Oliveros & Donea (2009) have examined the relationship between magnetic field changes and seismic emission in two acoustically active flares and found there was no a clear connection between the acoustic emission observed in the 5 - 7 mHz range and magnetic transients in one of the events, whilst in other flare the acoustic sources were found in the vicinity of the magnetic transients. They also note that there are many flares that show magnetic changes but no detectable acoustic emission. Thus, while it appears there are many common connections and overlaps in the phenomena described above, there are equally many unresolved questions regarding causal connections or not.

In this paper we present high resolution observations of the acoustically active flare of 14 December 2006. Our dataset comprises observations of the chromosphere and photosphere (including the magnetic field) from *Hinode* and TRACE; intensity and velocity data from the GONG (Global Oscillation Network Group) and HXR observations from RHESSI. This rather complete dataset provides us with an ideal opportunity to try to distinguish between the various contributions of the processes described above to the origin of flare acoustic emission. In § 2 we first outline the flare morphology and evolution at multiple wavelengths; discussing in § 2.2 the relationship between the various signatures seen in the photosphere and the chromosphere. In section § 3 we discuss the acoustic response of the flare obtained through the use of time-distance and acoustic holography methods. The associated helisoseismic velocity signatures are then compared with those measured by *Hinode* in the photosphere. We then present a summary of the observational signatures at various atmospheric depths. These signatures form the inputs for theoretical models (hydrodynamic, kinetic and radiative simulations) of the response of the lower atmosphere to particle precipitation during the flare that are discussed in Part II. In section 5 we present our conclusions and the requirements that the theoretical models must be able to account for.

2. Observations

2.1. Description of the data

The flare on 14 December 2006 originated from AR 10930 and occurred at approximately 22:00 UT. The X-ray flux for the event peaked at GOES X1.5 level around 22:12 UT. The event was observed by all the instruments on the *Hinode* spacecraft ((Kosugi et al. 2007)). In this paper we focus primarily on the observations made by the Solar Optical Telescope (SOT, Tsuneta et al. 2008). The SOT observed the flare throughout its duration with the Broad-band Filter Imager (BFI) in the G-band and Ca II H line, with a 2 minute cadence and 0.1 arcsec resolution. The Narrow-band Filter Imager (NFI) similarly provided Stokes I and V measurements with an approximately 2 minute cadence and 0.16 arcsec resolution in the Fe I 6302 Å line. Standard corrections were made to the data for CCD gain, readout defects, dark current and pedestal. The data were aligned using cross-correlation and sub-pixel registration on a large FOV similarly to the method described in Gosain et al. (2009). The alignment was verified through visual inspection of running difference images which showed random orientation of dipolar features within the FOV. Data from the spectropolarimeter (SP) were corrected for dark current, flat-field and cosmic rays with standard SolarSoft routines, and then inverted using the full atmosphere inversion code LILIA (Socas-Navarro 2001). The intrinsic 180° ambiguity was resolved using the Automated Ambiguity resolution code (AMBIG; Leka et al. (2009)) which is based on the Minimum Energy Algorithm (Metcalf 1994).

RHESSI observed the flare from its beginning until approximately 22:25 UT and we used the CLEAN algorithm to produce images at 1 minute time intervals from 22:08 - 22:15 UT, using the same procedure described by Watanabe et al. (2010).

GONG observations during the period were made in the photospheric Ni I 6768 Å line with 1 minute cadence. The observations included full disk Dopplergrams, line-of-sight magnetograms and intensity images. The pixel size of the intensity images is 2.5 arcsec. In this study we made use of the Dopplergrams and intensity images to analyze the acoustic signatures of the flare through both the time-distance diagram technique (TD method; Kosovichev & Zharkova 1998) and acoustic holography (e.g. Lindsey & Braun 2000). To compensate for atmospheric distortion we applied the cleaning procedures outlined in Lindsey & Donea (2008).

2.2. Flare morphology and evolution

The flare exhibited extended ribbon emission that propagated through the umbrae and penumbrae of both the Northern and Southern spots. This emission was seen in multiple wavelengths, as shown in Figure 1, where we plot a series of running difference images that display the temporal and spatial evolution of the flare in the G-band, the Stokes I and V components of the Fe I 6302 Å line, the Ca II H line and the TRACE WL channel. As can be seen from this Figure the morphology and location of the emission seen in the G-band and the Fe I 6302 Å Stokes I and V components is almost identical. The emission in the G-band is somewhat stronger than in the Stokes I and V components, but clear reversals of the field are seen in the Stokes V component, which can be considered to be a proxy for the line-of-sight magnetic field. TRACE's WL channel has a broad response which includes a contribution from the UV ((Fletcher et al. 2007)), and as a result the emission in this band is more extended than in the photospheric G-band and Fe I 6302 Å emissions. The Ca II H line difference images show that the photospheric emission forms a more compact subset of the chromospheric emission, but that it is spatially coincident. These observations clearly indicate that energy deposition at the photospheric level occurs over a more confined area than the overlying chromosphere.

In Figure 2 we illustrate the temporal evolution of the flare in the G-band and 40 - 100 keV HXR energy range in the Southern (diamonds) and Northern (asterisks) flare ribbons. The intensity has been normalized by area, but the strongest emission in the G-band is seen in the Southern ribbon, as also noted by Watanabe et al. (2010). Similarly, we note that the HXR intensity in the 20-30 and 40-100 keV bands is more intense in the South than the North. In Figure 3 we display images of the HXR emission reconstructed using the CLEAN algorithm in the 20 - 30 keV energy range. Overlaid on these images are contours of the 20 - 30 keV emission at the 50 and 70% level (black) and the 40 - 100 keV emission at the same levels (red). This demonstrates that as well as an asymmetry in intensity of the HXR sources, there is an asymmetry in size. In particular we note that the emission at 50 and 70% of the peak intensity in the 40 - 100 keV energy range in the Northern source is distributed over a much smaller area than the Southern source. It has been noted by e.g. Lindsey & Donea (2008) that the efficiency of photospheric heating in terms of exciting seismic emission wil be much greater if the heating is distributed over a compact region. Figure 4 illustrates the close spatial correspondence between the magnetic field transients, the G-band emission and the HXR emission in the South, while in Figure 5 we show the evolution of the magnetic field within the regions where the magnetic transients are observed (regions 1 and 4 in Figure 7) and the region where the strongest seismic source is observed (region 3 in Figure 7). We note that the field transient is slightly more impulsive in the South than the North, but primarily that in the region where the strongest seismic emission is seen there is an approximately 50% change that begins at 22:10 UT and is sustained for the following hour. However, it is a much noisier variation.

2.3. Underlying magnetic field configuration

SOT's SP performed fast map scans of the active region before, during and after the flare. The SP scans from East to West, and the scans began at 17:00 and 22:00 UT on the 14th December and 05:45 UT on the 15th. The FOV covered 1000 slit positions with a spatial resolution of $0.295x0.317$ arcseconds. The full polarization state (I, Q, U and V) of the Fe I 6301.5 and 6302.5 Å lines were obtained, allowing quantitative measurement of the vector magnetic field in the photosphere. As described in § 2 the data were inverted using the LILIA code (Socas-Navarro 2001) and the azimuth ambiguity was resolved using the Automatic Ambiguity Resolution code. In Figure 6 we show the absolute magnetic field strength in the active region at 17:00 (top left), 22:00 (top center) and 05:45 UT (top right) and the magnetic field inclination with respect to the line of sight at the same times. An inclination of 90° indicates a field perpendicular to the line of sight direction. The boxes show the locations of the seismic and HXR sources. It can be seen that there are significant changes within the active region during the period of the three scans, which is some 12 hours in total. Clearly the length of time taken to scan the region makes it difficult to say with certainty which changes occur as a direct result of the flare, and which are dues to 'normal' active region evolution. However, we note that while inclined magnetic field is seen in both parts of the active region where the seismic sources are observed, the field appears to be significantly more vertical in the North than in the South. In terms of magnetic field strength, the regions in which the seismic sources occurred show a mix of field strengths, with the majority ranging between 1000 - 2000 Gauss. Prior to the flare, the region in the North includes a number of small-scale concentrations of higher field strength, approaching

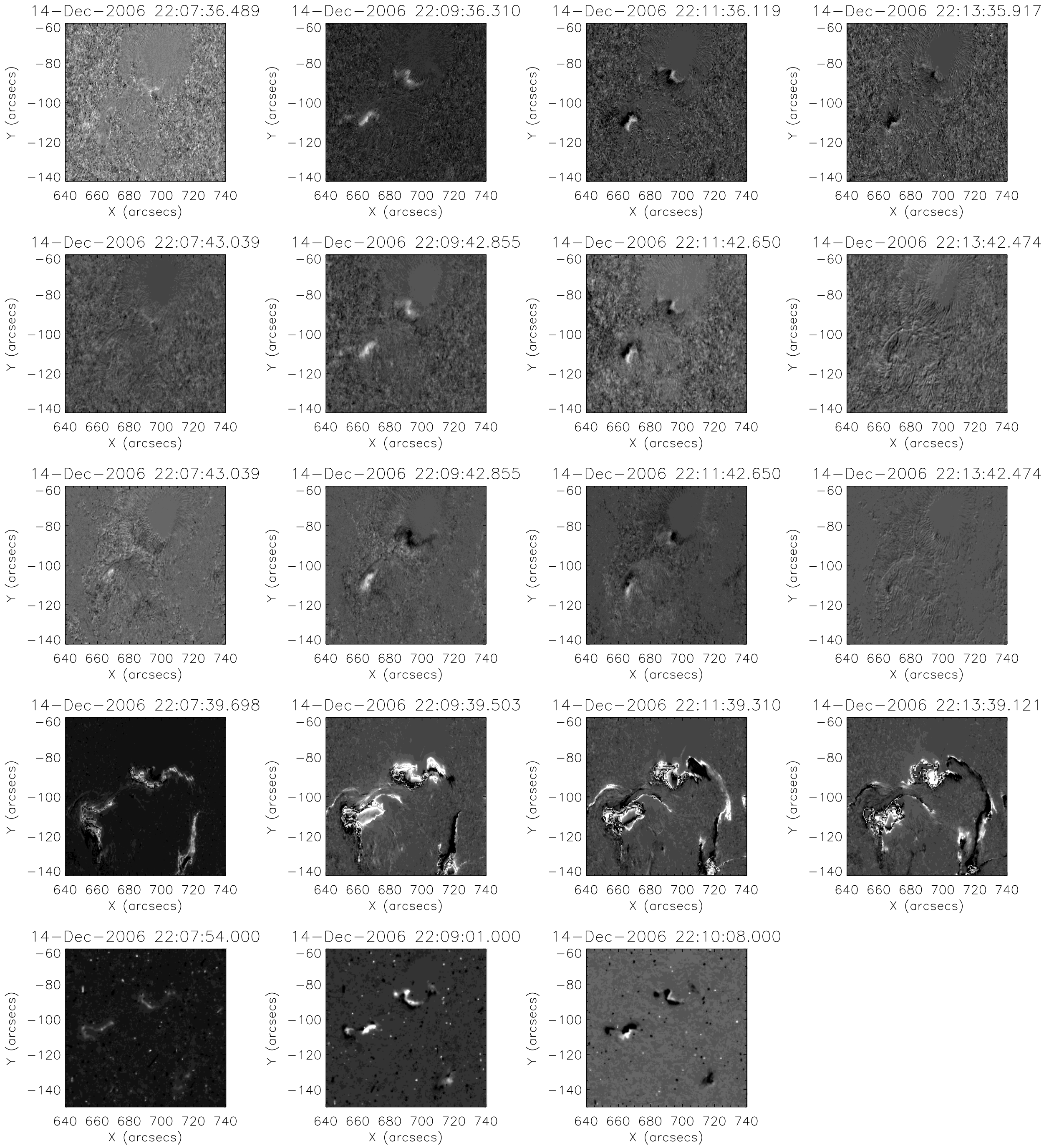

Fig. 1.— In descending order: G-band running difference; Fe I intensity running difference; Fe I Stokes V running difference; Ca II H running difference; TRACE WL running difference.

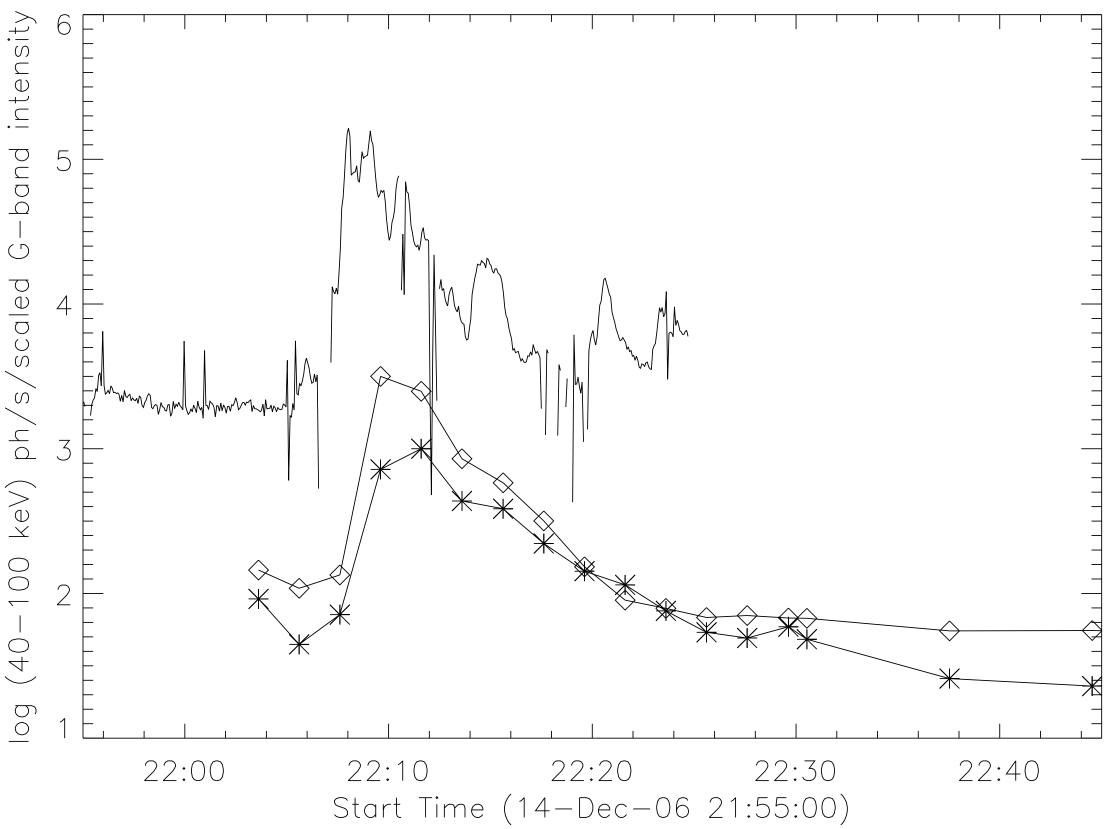

Fig. 2.— Temporal evolution of the 40-100 keV HXR emission (solid line) and G-band emission in the South ribbon (diamonds) and in the North ribbon (asterisks). The intensity has been scaled to aid visual comparison of the curves.

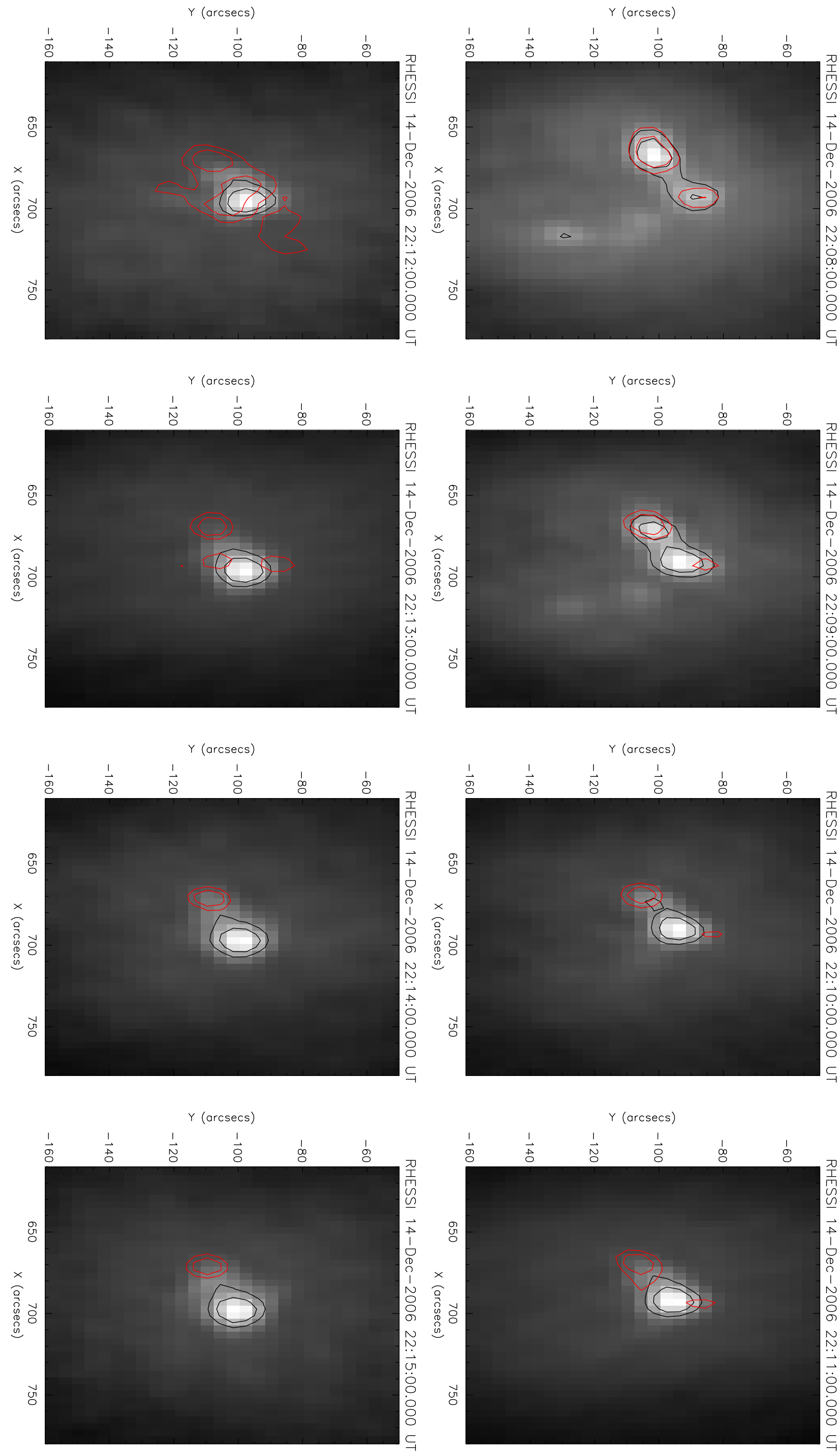

Fig. 3.— Timeseries of HXR images from 22:08 - 22:15 UT on 14 December 2006. The grey-scale images are 20 - 30 keV, with overlying contours (black) showing the emission at 50 and 70% of the peak. The red contours show the 40 - 100 keV emission at the same levels.

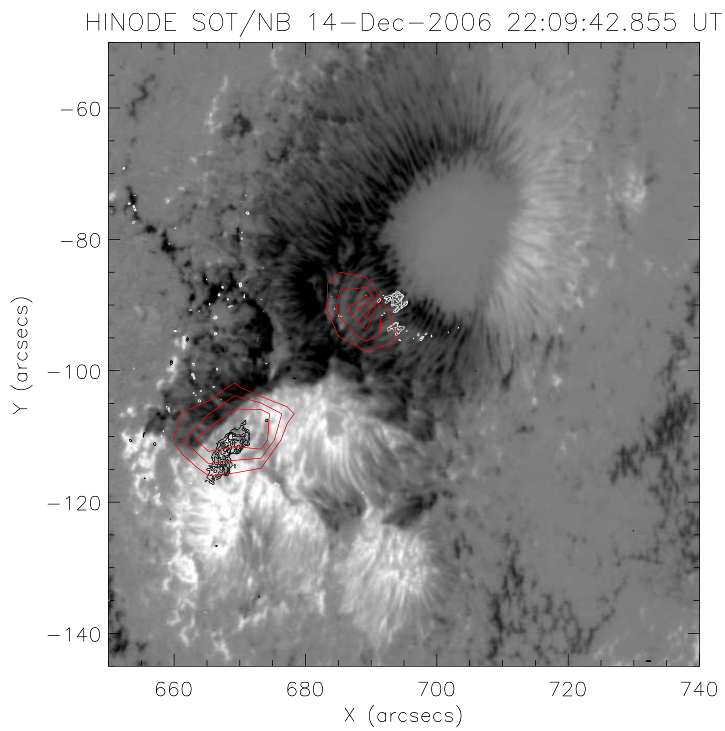

Fig. 4.— Stokes V image showing the location of 50-100 keV HXR emission seen by RHESSI (red contours) and the magnetic reversals (black and white contours).

4000 Gauss, while in the South there a larger concentrations of similar field strength at the edge of region of interest. During the flare, we note that in the North, fewer but larger regions of high field strength are seen, while in the South there is a significant enhancement of the high flux region to the North-East of the region of interest. Following the flare the field in the North is sigificantly weakened, while concentrations of strong field remain in the South.

2.4. Photospheric velocities

Hinode's SOT also allows us to investigate how the photospheric velocity field changes during the course of the flare. The region, as noted above, was observed at approximately 2 minute cadence by both the NFI and the BFI. The SP also performed a scan of the region, as we describe above, but unfortunately did not cover the flare region until 22:35 UT, well after the impulsive phase and the onset of the quake. We are therefore unable to discern any significant Doppler velocities in the location of the seismic sources during using these data. However, the observations from the NFI do offer us the opportunity to investigate how the horizontal velocities vary during the flare and in response to the quake.

We follow a similar procedure to that described in Gosain et al. (2009) and take a sequence of Stokes V images taken in the Fe I 6302 Å line in the period from 21:47 -23:40 UT. Using the whole field of view we registered this image series to the first image in the time series using cross-correlation and sub-pixel interpolation (e.g November & Simon (1988)). While, as Gosain et al. (2009) note, small-scale features will evolve from frame to frame given the 2 minute cadence of the observations, the large-scale features such as the spots will not. This method thus gives us a good global co-alignment that allows us to investigate small-scale changes. In order to satisfy ourselves that the co-alignment was good, we examined difference images to ensure that there was no systematic alignment of the orientation of dipolar feature, as would be expected from an error in the correlation.

Having performed the global alignment of the time sequence we then looked at frame-to-frame changes in small regions centered on the locations of the largest changes associated with the magnetic changes, HXR and acoustic sources, as indicated in Figure 7. We also selected a region in the SW of the active region away from the flare emission as a reference. We again used cross-correlation with sub-pixel interpolation between consecutive frames to determine the displacements Δx and Δy of the small-scale features within the boxes. These displacements are then converted to velocities as shown in Figure 8.

Regions 1 and 2 as seen in Figure 7 represent the locations associated with strongest

G-band and HXR source in the Southern spot, and the greatest change in Stokes V. The velocities associated with these locations indicate a sharp decrease in v_x at approximately 22:10 UT, consistent with the derived onset time of the solar quake, and a corresponding increase in v_y. In region 2, an increase in v_y is also seen, but somewhat earlier, followed by a swing to negative velocities at the time of the quake onset. v_y magnitudes range from -0.7 to 1.5 kms^{-1}, compared with v_x = -0.5 to 0.2 kms^{-1}. In region 3, which represents the best match to the location of the Northern seismic source seen with time-distance (TD) technique, we see that there is no obvious signature of the flare in v_x. However, a sharp decrease in v_y is seen at the time of the quake onset. We note that in this case there is a more gradual return to the pre-flare velocity levels over some 30 minutes, in contrast to regions 1 and 2. Region 4, located in the region of largest change in Stokes V in the Northern flare ribbon, displays a swing in both v_x and v_y consistent with the time of the quake. Velocities in this region show the greatest change with v_x ranging from -2.5 to 0.2 kms^{-1}, v_y ranges between -0.3 to 0.5 kms^{-1}. Comparison with region 5, which is unaffected by the flare, demonstrates that the increases in velocities seen in regions 1-4 are significant.

3. Observations in the solar interior

3.1. Description of basic techniques

Since there are no suitable SOHO MDI observations available during the flare period we have obtained intensity and dopplergram data from the GONG network (Harvey et al. 1996). Both data sets used in our analysis consist of several hours of full-disk one minute cadence intensity and line of sight velocity observations starting at 22:00UT, December 14, 2006. Each series were processed by tracking and de-rotating the region of interest centered on the active region using the Snodgrass rotation rate, and then remapping the data onto heliographic grid at 0.15° per pixel resolution. Also, as GONG is ground-based, the data are affected by visibility conditions at the time of observation. To compensate for this we use the cleaning procedures described in Lindsey & Donea (2008) for GONG intensity data. Since both intensity and velocity data come from the same instrument, we apply the parameters extracted from the intensity series to correct the line of sight velocity data.

In order to detect and analyze the solar quake associated with the flare we use both time-distance analysis (Kosovichev & Zharkova 1998) and acoustic holography (Donea et al. 1999). Time-distance analysis is applied to detect the spherical wave packet generated by the quake. This consists of rewriting the observed surface signal in polar coordinates relative to the source, i.e. $v(r, \theta, t)$, and using azimuthal transformation

$$V_m(r,t) = \int_0^{2\pi} v(r,\theta,t) e^{-im\theta} d\theta,$$

to study the $m = 0$ component for evidence of the propagating wave. Then if seen, the quake manifests itself as a time-distance ridge, thus providing estimates of the surface propagation speed and the time of excitation. In this work the GONG high-cadence velocity data were used in the time-distance analysis.

Acoustic holography is applied to calculate the egression power maps from observations. The holography method (Braun & Lindsey 1999; Donea et al. 1999; Braun & Lindsey 2000; Lindsey & Braun 2000) works by essentially "backtracking" the observed surface signal, $\psi(\mathbf{r}, t)$, by using Green's function, $G_+(|\mathbf{r} - \mathbf{r}'|, t - t')$, which prescribes the acoustic wave propagation from a point source. This allows us to reconstruct egression images showing the subsurface acoustic sources and sinks:

$$H_+(\mathbf{r}, z, t) = \int dt' \int_{a<|\mathbf{r}-\mathbf{r}'|<b} d^2\mathbf{r}' G_+(|\mathbf{r} - \mathbf{r}'|, t - t')\psi(\mathbf{r}', t'),$$

where a, b define the holographic pupil. The egression power is then defined as

$$P(z, \mathbf{r}) = \int dt |H_+(\mathbf{r}, z, t)|^2 dt$$

In this work, Green's functions built using a geometrical optics approach were used, pupil dimensions were defined $a \approx 15$ Mm, $b \approx 55$ Mm, with GONG continuum intensity data taken as $\psi(\mathbf{r}, t)$ for the egression power calculations.

3.2. Validation of time-distance analysis with GONG

As we are not aware of the time-distance method ever having been applied to GONG data before, we have tested the approach using the M9.5 type flare associated with active region NOAA 9608 that occurred September 9, 2001. For this flare both GONG and SOHO/MDI (Scherrer et al. 1995) line-of-sight velocity data were available. Using acoustic holography, Donea et al. (2006) detected and reported the seismic emissions associated with this M-class flare taking place from 20:40 UT to 20:48 UT.

Both datasets were processed as described above, followed by the additional frequency filtering to select the signal in 2 mHz band centered at 6 mHz. Using the fact that the ridge we are looking for corresponds to the first bounce acoustic wave-packets normally seen in the interval from 15 to 150 Mm from the source, to improve sensitivity of the technique for GONG data, we also applied a phase-speed type filter designed to let through waves with phase-speed, $\frac{\omega}{k_h}$, between 20 and 90 km/s unaffected with a Gaussian roll-off on each side. The time-distance diagrams for the $m = 0$ component are presented in Figure 9 for both observatories. The ridge representing the quake is clearly seen in the MDI image. By comparing this with GONG time-distance diagram one can also detect there a disturbance located at the same part of the image. Though less defined and obscured by a significant noise contribution, nevertheless, the ridge is definitely present. Thus, we conclude that GONG network data, though less sensitive to time-distance technique, still can respond to such the analysis, i.e. if a ridge is seen in this ground-based data it will also be observed by using the higher-quality satellite MDI data.

3.3. December 14, 2006, helioseismic results

The time distance plots (Figure 10, left) computed from the GONG dopplergrams at the location around 8.4° Carrington longitude and 5.25° latitude South, show a ridge corresponding to the propagation of the spherical acoustic wave excited by the flare that occurred at these coordinates. The position corresponds to the Northern egression source and is spatially coincident with the strong HXR source in this location. The ridge is fitted well by the theoretical ridge (Figure 10, centre) corresponding to spherical wave number $l = 1000$, with the quake start time estimated at around 22:10 UT.

Perhaps due to the atmospheric contribution present in the GONG velocity observations, we are not able to reliably distinguish an acoustic source at the second (South) location using the time-distance method. However, the egression power, shows two sources (North and South), approximately coincident with the HXR source locations (see Figure 11). Hence, for the Southern acoustic source location we use the acoustic holography technique, which appears to be a more sensitive to noisy signals present in dopplergrams when using even the better quality SOHO MDI data, thus detecting greater number of quakes (see for the instance Donea & Lindsey 2005; Besliu-Ionescu et al. 2005; Lindsey & Donea 2008). The peak of egression power in the Southern acoustic source coinciding with the strongest HXR source in this flare is observed around 22:07-22:08 UT, e.g. just at the start of HXR emission (see Figure 2). However, due to the filtering in 5-7 mHz frequency band used in processing as advised for GONG data (Donea & Lindsey 2005), the egression power signatures are smeared by ≈ 500 s.

4. Discussion

In this study we present high resolution multi-wavelength signatures of an X-class solar flare accompanied by a sun-quake, including the first detection of a quake in GONG data by time-distance methods. Our motivation for this study was to explore the connections between chromospheric, photospheric and sub-photospheric signatures of flares to try to clarify the physical mechanisms by which they are produced. In particular, there has been a great deal of debate recently in the literature regarding the relative roles of chromospheric shocks, backwarming and Lorentz force transients in accounting for the seismic emission observed during solar quakes. In these observations we find that there is generally a good spatial and temporal coincidence between photospheric emission as observed in the G-band and the Fe I 6302 Å line, transient changes in the line-of-sight magnetic field and HXR emission. These signatures also correlate well spatially and temporally with the acoustic sources detected in the GONG data, with the peak of the HXR emission and the quake onset being coincident within the uncertainties of the time-distance method. However, there are some surprising findings which we highlight below.

We find that the photospheric emission is more compact than the emission seen in the chromosphere, particularly in the TRACE WL and Ca II H observations, indicating that the energy deposition at this level occurs over smaller scales, consistent with findings by e.g. Fletcher et al. (2007). In agreement with Watanabe et al. (2010) we find that the HXR emission is asymmetric, with stronger emission in the HXR, G-band and the Stokes V component of the Fe I 6302 Å line being seen in the South source. The onset of the flare-related signatures also appears to occur earlier and to be more impulsive in the South, within the temporal resolution of the available data. We see also that, while there is a good spatial correspondence between the G-band, Stokes V and HXR emission and the egression power in the South, the seismic signature is weakest here. The Northern seismic source shows good spatial and temporal agreement with the 20 - 30 keV HXR emission and is located at the Eastern end of the G-band ribbon. The 40 - 100 keV HXR emission is located further North than both the 20 -30 keV HXR and the seismic emission. It is well correlated in space and time with the strongest magnetic transient in the North, and we note that it is spatially more compact than the 40 -100 keV emission in the South. Energy deposition per unit area is an important factor in determining the efficiency in the production of acoustic emission as noted by Lindsey & Donea (2008), but in this case there seems to be a much better corrleation with the lower energy HXR emission. A similar asymmetry in HXR intensity was also noted by Lin et al. (2003) in the 23 July 2002 flare with the HXR sources spatially moving during the flare duration. Lin et al. (2003) also reported the appearance in γ-ray sources in the very different locations from HXR sources, and this flare was also later investigated by Kosovichev (2007) for the presence of weak asymmetric seismic sources whose locations were consistent with the γ-ray sources.

Observations from the SP indicate that the underlying magnetic field strength is mixed within the regions where the seismic sources occur, with the largest number of strong field concentrations ($>$ 3000 Gauss) occurring predominantly in the vicinity of the Southern source. The field inclination is also mixed within the vicinity of both sources, but with more inclined field seen in the South. Martínez-Oliveros et al. (2008a) highlight the importance of strong and inclined magnetic field from the point of view of helioseismic signatures, since mode conversion will occur more effectively when the sound and Alfvén speeds coincide. From this perspective we would expect that the seismic signature would be stronger in the South than in the North.

We have examined the variation of horizontal velocity in the photosphere using frame-to-frame cross-correlation of the Stokes V images in regions centred on the strongest flare emission. We find that there are clear signatures in these velocities coincident with the onset of the quake. In particular, these signatures are largest in the North where the strongest magnetic signature is seen. Here we see large relative changes in both v_x and v_y with a swing to negative velocities first of all in v_x, followed by a return to almost pre-flare levels and then a much greater change (250%) back to negative velocities that coincides with the HXR peak and quake onset between 22:07 and 22:10 UT. In v_y we see an increase towards the positive velocity direction followed by a similar return, then another increase to positive velocities and swing to the negative. In both cases, the velocities have returned to the pre-flare levels by 22:20 UT. In contrast, in region 3 (Figure 7), which coincides spatially with the seismic source in the North, we see no coherent change in v_x, but a sharp drop in v_y which begins around 22:00 UT and reaches its minimum at approximately the time of the quake onset. These velocities show a more gradual return to pre-flare values over some 40 minutes. In the South (regions 1 and 2) we see sharp spikes in both v_x and v_y at the time of the quake onset, with a series of swings in v_x, in particular, including the second sharp change at approximately 22:20 UT.

We recognize that since we detect polarity reversals in these regions, it might be considered that these changes purely reflect the change in intensity of the emission. However, we note first of all that the changes in Stokes V intensity shown in Figure 5 do not show the complicated type of behaviour that we see in the v_x and v_y plots; secondly, that a close inspection of the associated images suggests that there is a clear change in the underlying structures; and thirdly that creating a change in horizontal motion at the photospheric level requires a large deposition of momentum that cannot be produced by non-thermal processes and heating alone. We, thus, believe that these changes are most likely to be produced by shocks rather than as the artifacts of changes in the line emission caused by non-thermal particle bombardment or heating alone.

5. Conclusions

In summary, from the observations presented we find the following:

1. The flare exhibited extended ribbon emission that propagated through the umbrae and penumbrae of both the Northern and Southern spots and was seen at multiple wavelengths and levels in the chromosphere and photosphere.

2. The emission in the G-band is somewhat stronger than in the Stokes I and V components of the Fe I 6302 Å line, but the morrphology is similar and clear reversals of the field are seen in the Stokes V component, which can be considered to be a proxy for the line-of-sight magnetic field.

3. TRACE's WL emission is more extended than in the photospheric G-band and Fe I 6302 Å emissions. The Ca II H line difference images show that the photospheric emission forms a more compact subset of the chromospheric emission, but that it is spatially coincident. These observations clearly indicate that energy deposition at the photospheric level occurs over a more confined area than the overlying chromosphere.

4. The HXR intensity in the 40-100 keV bands is more intense in the South than the North, but the intensity in the 20 - 30 keV band is stronger in the North. There is also an asymmetry in source size in the 40 - 100 keV band, with the emission at 50 and 70% of the peak intensity in this energy range distributed over a much smaller area in the Northern than the Southern source.

5. The time distance diagrams computed from the GONG dopplergrams at the location around 8.4° Carrington longitude and 5.25° latitude South (Northern source), show a ridge corresponding to the propagation of the spherical acoustic wave excited by the flare. This position is spatially coincident with the strong HXR source in this Northern source. The ridge is fitted well by the theoretical ridge corresponding to spherical wave number $l = 1000$, with the quake start time estimated at about 22:10 UT. We are not able to reliably distinguish an acoustic source at the second (South) location by using time-distance method.

6. The egression power analysis shows the two sources (North and South), approximately coincident with the HXR source locations. The peak of egression power in the Southern

acoustic source, coinciding with the strongest HXR (40 - 100 keV) source in this flare is observed around 22:07-22:08 UT, e.g. just at the start of HXR emission.

7. The location of the North seismic source is poorly correlated with the 40 - 100 keV HXR emission, strongest G-band emission and magnetic transient, but well correlated with the 20 -30 keV HXR emission.

8. The underlying magnetic field strength in the regions associated with the acoustic sources is mixed, but shows a larger concentration of high field strength (> 3000 G) in the South than the North. There are significant changes in distribution of the field in these regions during the 12 hours that encompass the flare. The inclination of the magnetic field in these regions is also mixed, but there is more inclined field in the South than the North. During the time that the SP scanned the region during the flare (22:30 UT) there are new regions of inclined field visible in the North.

9. Regions 1 and 2, representing the locations associated with strongest G-band and HXR emission in the southern seismic source and the greatest change in Stokes V, reveal a sharp decrease in v_x at approximately 22:07 - 22:08 UT, consistent with the time of peak egression power in the Southern seismic source and a corresponding increase in v_y. In region 2, an increase in v_y is also seen, but somewhat earlier, followed by a swing to negative velocities at the time of the quake onset. v_y magnitudes range from -0.7 to 1.5 kms^{-1}, compared with v_x = -0.5 to 0.2 kms^{-1}.

10. In region 3, which represents the best match to the location of the Northern seismic source, we see that there is no obvious signature of the flare in v_x. However, a sharp decrease in v_y is seen at the time of the quake onset. We note that in this case there is a more gradual return to the pre-flare velocity levels over some 40 minutes, in contrast to regions 1 and 2.

11. Region 4, located coincident with the strongest magnetic transient in the North, displays a swing in both v_x and v_y coincident with the time of the quake.

12. The underlying magnetic field strength in region 4 is greater than in either of the regions where the egression and time-distance sources are located, but less inclined.

In this study we have, to our knowledge, presented the first detection of a solar quake from GONG data using time-distance methods. We have examined in detail the associated flare responses in the photosphere and the chromosphere in order to try to determine the origins of the quake in the context of current ideas. Our findings are somewhat surprising in the sense that, while we find general good agreement between the location and timing of the photospheric and chromospheric flare signatures (G-band, Fe I 6302 Å and HXR) and the seismic sources, we see a pronounced asymmetry in the intensity of these responses which does not fit with our expectations for the strength of the associated seismic sources. That is, we find higher intensity HXR (at 40 - 100 keV) and G-band emission and a more impulsive change in Stokes V intensity associated with the Southern seismic source, but a weaker seismic signal. In addition the underlying photospheric magnetic field in this location contains a larger concentration of inclined and high strength (> 3000 G) magnetic field than the region in the North. From previous work in this area (e.g. Martínez-Oliveros et al. (2008a) and references therein) we would expect that stronger HXR emission and strong and inlined magnetic field that shows an impulsive change in flux would coincide with a strong seismic source.

The location of the North seismic source (region 3), which is the stronger of the two, also agrees well with the location of the HXR emission, but is better correlated with the source in the lower energy 20 -30 keV band than the higher energy band. The 40 - 100 keV HXR emission is offset and corresponds well with the G-band and Fe I 6302 Å signatures, including the magnetic transient. These signatures in the Northern flare ribbon are also somewhat unexpected. While we do see a change in the underlying field strength and inclination, as well as in magnetic flux in this region (region 3), they are much less pronounced effects than at the Western end of the flare ribbon (region 4) and in the Southern ribbon. This may suggest that in this instance the contribution of magnetic field changes is not a significant contribution to the quake origin in this location. Shelyag et al. (2009) have recently studied the effects of magnetic tension on acoustic wave propagation in sunspots and find that in strong field there can be strong suppression of the acoustic motions, particularly when the field is highly curved, and that a more complicated response is seen in weakly curved strong field. It may be that the very high field strengths in the region of the magnetic transient (Region 4) are leading to suppression of the seismic response here. One further possibility in terms of accounting for the asymmetry of the acoustic sources may lie in different characteristics of the hydrodynamic shocks associated with different particle beam properties in the North and the South. In Part II we explore these possibilitis further and present hydrodynamic modelling based on the observations reported here.

Hinode is a Japanese mission developed and launched by ISAS/JAXA, with NAOJ as domestic partner and NASA and STFC (UK) as international partners. It is operated by these agencies in co-operation with ESA and NSC (Norway). We thank Santiago Vargas Dominguez for help in processing the SOT SP data.

REFERENCES

Besliu-Ionescu, D., Donea, A., Cally, P., & Lindsey, C. 2005, in ESA Special Publication, Vol. 600, The Dynamic Sun: Challenges for Theory and Observations

Braun, D. C. & Lindsey, C. 1999, ApJ, 513, L79

Braun, D. C. & Lindsey, C. 2000, Sol. Phys., 192, 285

Donea, A., Besliu-Ionescu, D., Cally, P. S., Lindsey, C., & Zharkova, V. V. 2006, Sol. Phys., 239, 113

Donea, A., Braun, D. C., & Lindsey, C. 1999, ApJ, 513, L143

Donea, A. & Lindsey, C. 2005, ApJ, 630, 1168

Edelman, F., Hill, F., Howe, R., & Komm, R. 2004, in ESA Special Publication, Vol. 559, SOHO 14 Helio- and Asteroseismology: Towards a Golden Future, ed. D. Danesy, 416–+

Fletcher, L., Hannah, I. G., Hudson, H. S., & Metcalf, T. R. 2007, ApJ, 656, 1187

Gosain, S., Venkatakrishnan, P., & Tiwari, S. K. 2009, ApJ, 706, L240

Harvey, J. W., Hill, F., Hubbard, R. P., et al. 1996, Science, 272, 1284

Hudson, H. S., Fisher, G. H., & Welsch, B. T. 2008, in Astronomical Society of the Pacific Conference Series, Vol. 383, Subsurface and Atmospheric Influences on Solar Activity, ed. R. Howe, R. W. Komm, K. S. Balasubramaniam, & G. J. D. Petrie , 221–+

Kosovichev, A. G. 2006, Sol. Phys., 238, 1

Kosovichev, A. G. 2007, ApJ, 670, L65

Kosovichev, A. G. & Zharkova, V. V. 1995, in ESA Special Publication, Vol. 376, Helioseismology, 341–+

Kosovichev, A. G. & Zharkova, V. V. 1998, Nature, 393, 317

Kosovichev, A. G. & Zharkova, V. V. 2001, ApJ, 550, L105

Kosugi, T., Matsuzaki, K., Sakao, T., et al. 2007, Sol. Phys., 243, 3

Leka, K. D., Barnes, G., Crouch, A. D., et al. 2009, Sol. Phys., 260, 83

Lin, R. P., Krucker, S., Hurford, G. J., et al. 2003, ApJ, 595, L69

Lindsey, C. & Braun, D. C. 2000, Sol. Phys., 192, 261

Lindsey, C. & Donea, A. 2008, Sol. Phys., 251, 627

Martínez-Oliveros, J. C. & Donea, A. 2009, MNRAS, 395, L39

Martínez-Oliveros, J. C., Donea, A., Cally, P. S., & Moradi, H. 2008a, MNRAS, 389, 1905

Martínez-Oliveros, J. C., Moradi, H., & Donea, A. 2008b, Sol. Phys., 251, 613

Metcalf, T. R. 1994, Sol. Phys., 155, 235

November, L. J. & Simon, G. W. 1988, ApJ, 333, 427

Qiu, J. & Gary, D. E. 2003, ApJ, 599, 615

Qiu, J., Lee, J., Gary, D. E., & Wang, H. 2002, ApJ, 565, 1335

Scherrer, P. H., Bogart, R. S., Bush, R. I., et al. 1995, Sol. Phys., 162, 129

Shelyag, S., Zharkov, S., Fedun, V., Erdélyi, R., & Thompson, M. J. 2009, A&A, 501, 735

Socas-Navarro, H. 2001, in Astronomical Society of the Pacific Conference Series, Vol. 236, Advanced Solar Polarimetry – Theory, Observation, and Instrumentation, ed. M. Sigwarth, 487–+

Sudol, J. J. & Harvey, J. W. 2005, ApJ, 635, 647

Tsuneta, S., Ichimoto, K., Katsukawa, Y., et al. 2008, Sol. Phys., 249, 167

van den Oord, G. H. J. 1990, A&A, 234, 496

Watanabe, K., Krucker, S., Hudson, H., et al. 2010, ApJ, 715, 651

Wolff, C. L. 1972, ApJ, 176, 833

Zharkova, V. V. 2008, Sol. Phys., 251, 641

Zharkova, V. V. & Gordovskyy, M. 2006, ApJ, 651, 553

Zharkova, V. V. & Kosovichev, A. G. 2002, in ESA Special Publication, Vol. 506, Solar Variability: From Core to Outer Frontiers, ed. J. Kuijpers, 1031–1034

Zharkova, V. V. & Zharkov, S. I. 2007, ApJ, 664, 573

Zharkova, V. V., Zharkov, S. I., Ipson, S. S., & Benkhalil, A. K. 2005, Journal of Geophysical Research (Space Physics), 110, 8104

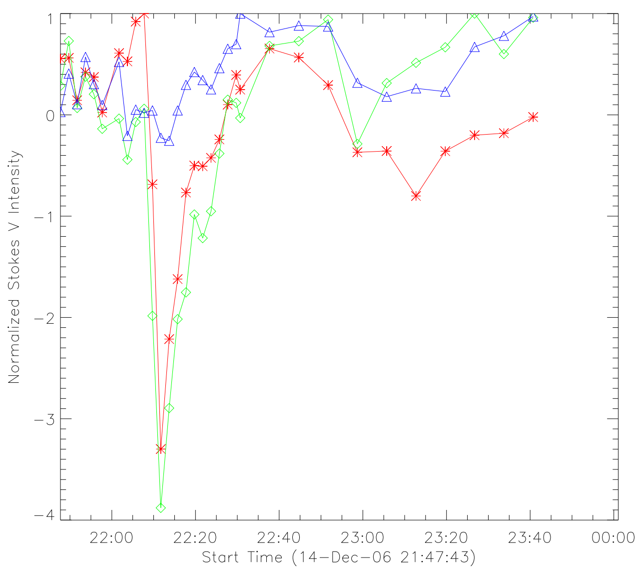

Fig. 5.— Normalized Stokes V intensity in regions 1 (asterisks), 3 (triangles) and 4 (diamonds) as indicated in Figure 7.

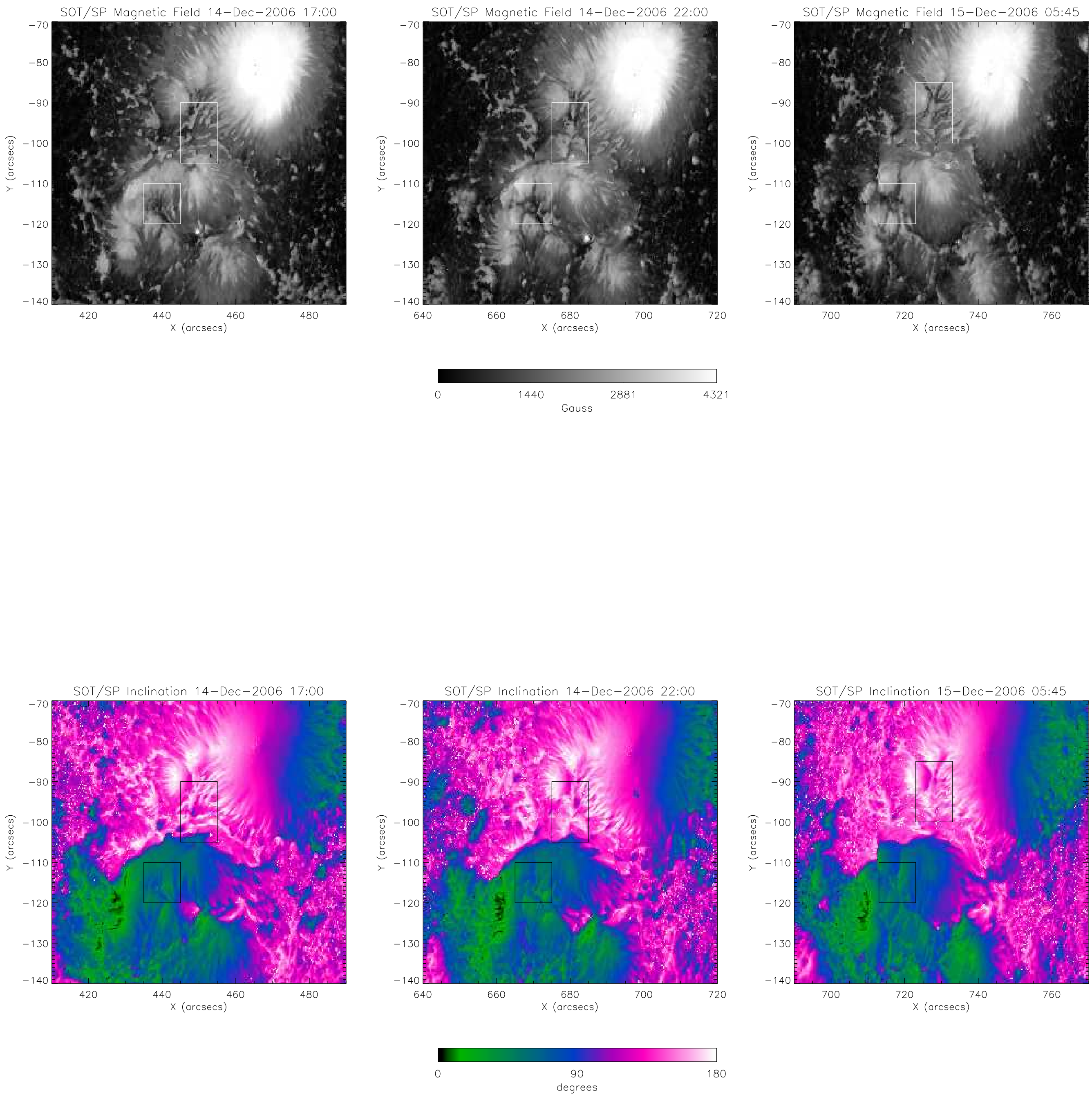

Fig. 6.— Top: absolute magnetic field strength in Gauss at 17:00 (left) and 22:00 UT (center) on the 14th December 2006, and 05:45 UT (left) on the 15th December. Bottom: magnetic field inclination at corresponding times. The boxes represent the locations of the acoustic and HXR sources.

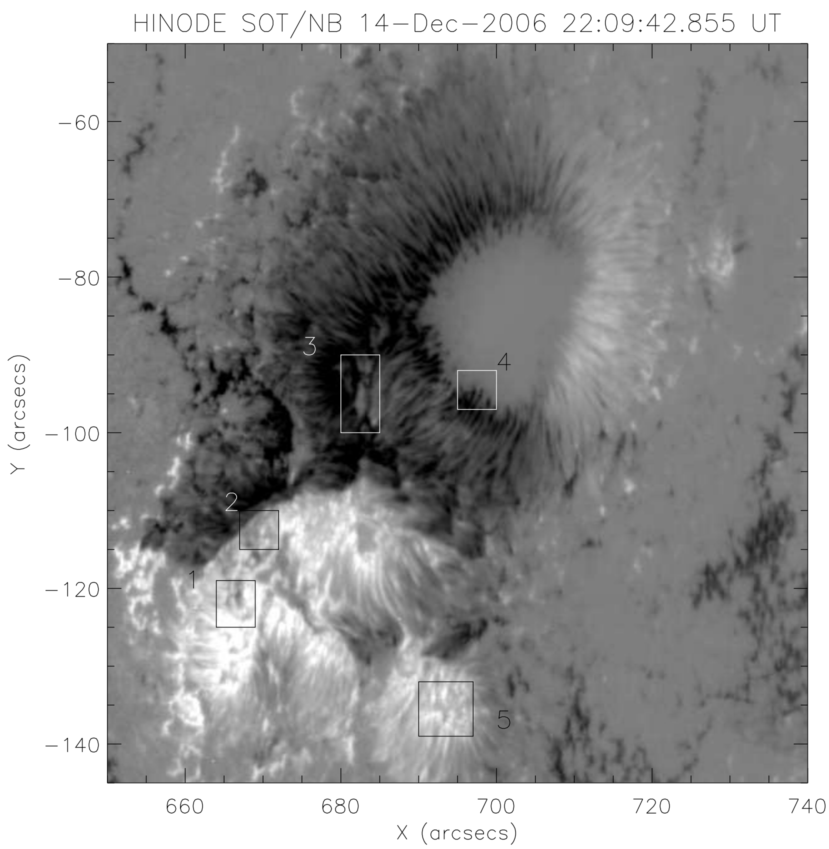

Fig. 7.— Stokes V image at 22:09 UT, indicating the regions where magnetic variations and photospheric velocities were measured. Magnetic variations where measured in regions 1,2 and 4. Horizontal photospheric velocities were measured in all five regions, with region 5 providing a reference location outside of the main flare disturbance.

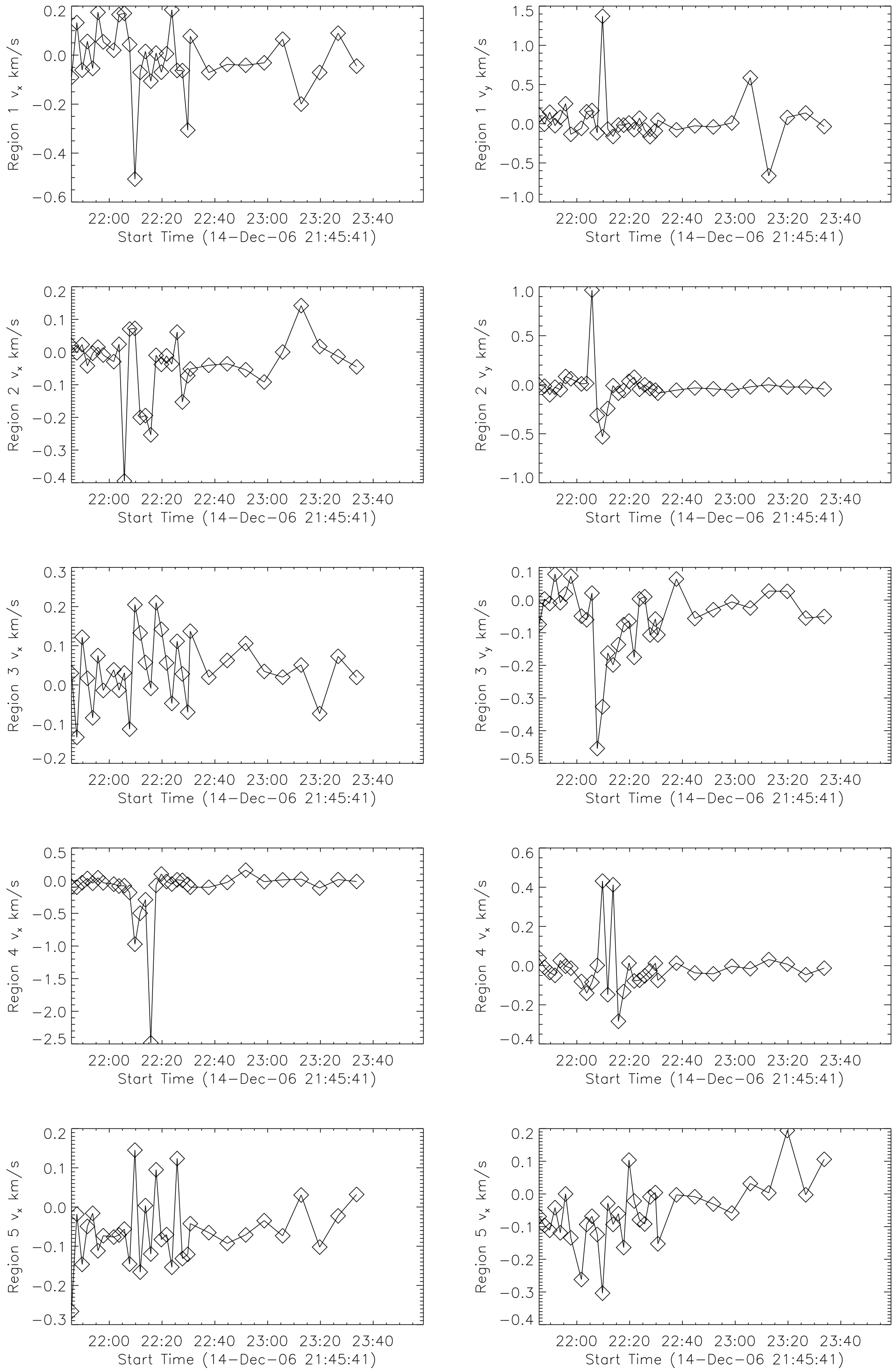

Fig. 8.— Horizontal velocities derived from the displacements measured in the regions shown in Figure 7. Left panels show v_x and right v_y.

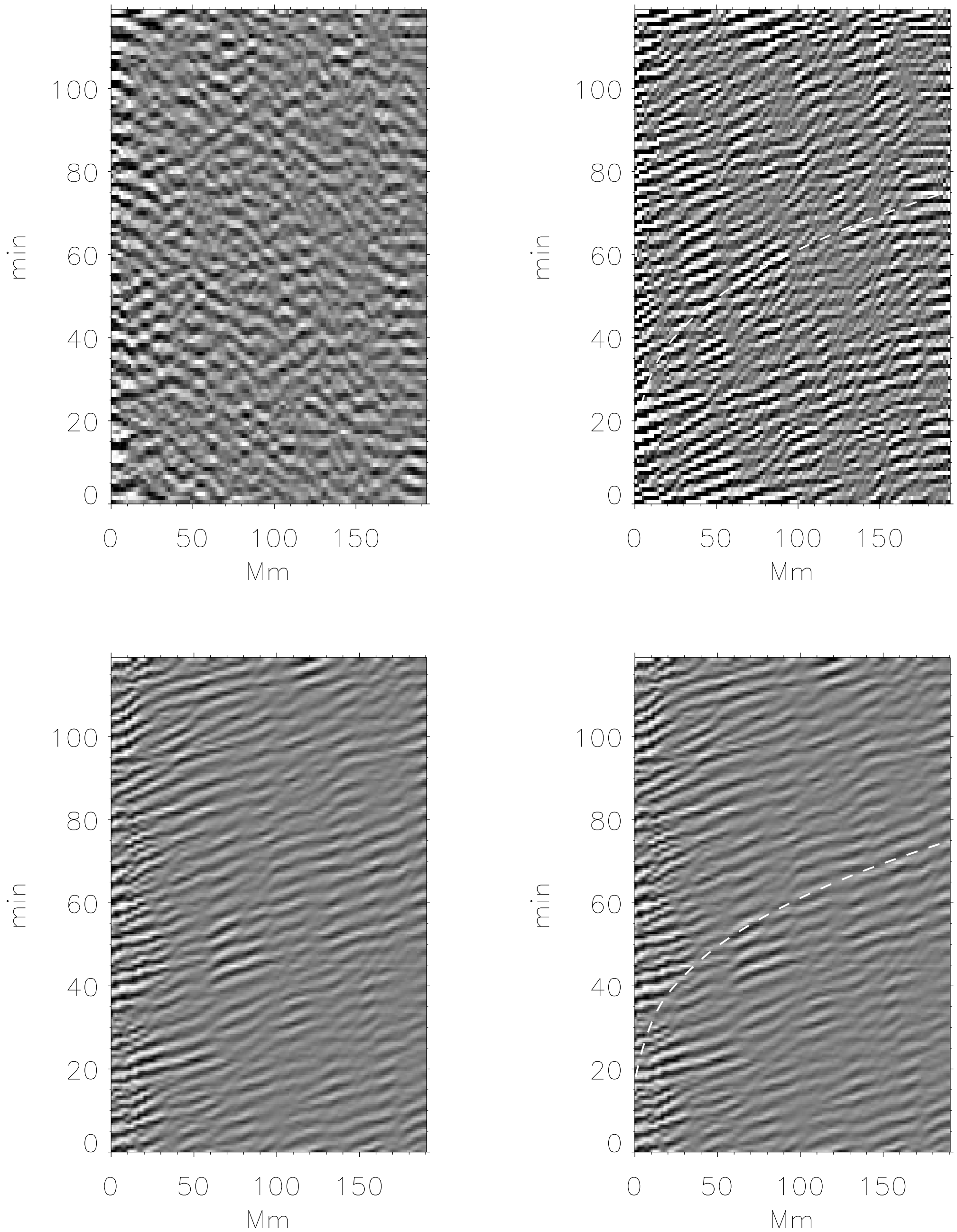

Fig. 9.— Comparison of time-distance diagrams extracted from MDI *(top row)* and GONG *(bottom row)* data for September 9, 2001, M-class flare. The x-axis represents radial distance from the source, y-axis is labeled in minutes since 20:30UT, September 9, 2001. The top left figure shows unfiltered time-distance diagram obtained from MDI data. Next to the right, the same diagram from MDI data filtered using a 2 mHz wide bandpass frequency filter centered at 6 mHz. Over-plotted is the theoretical time-distance curve derived from the unfiltered data. The bottom left plot presents the time-distance diagram from GONG data obtained using the same bandpass filter in combination with a wide phase speed type filter as described in the text. The last image is the same GONG diagram with the theoretical time-distance curve over-plotted.

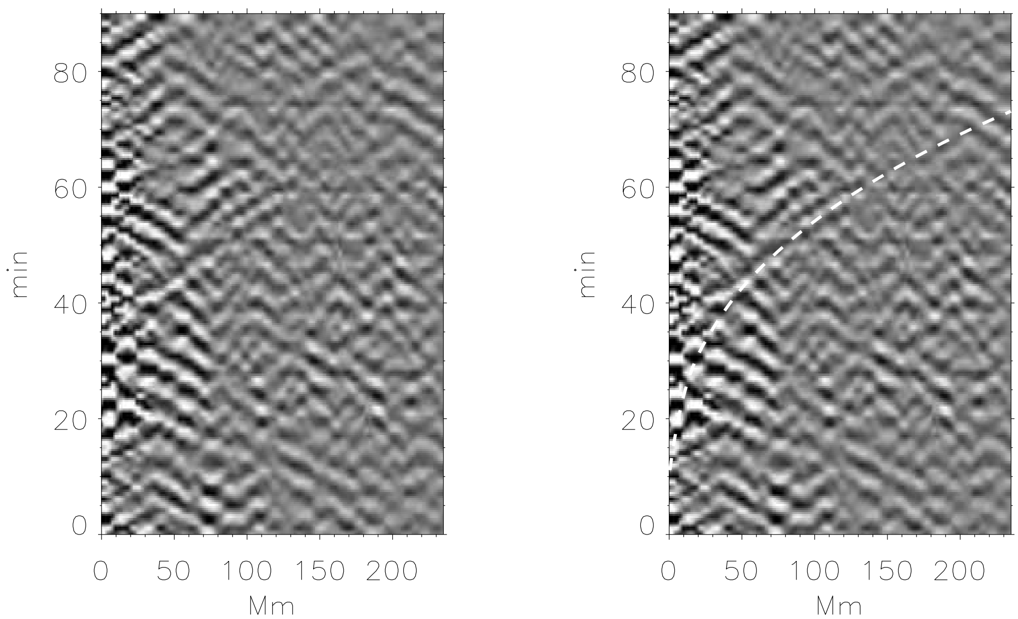

Fig. 10.— Time-distance diagram for the northern source *(left)* with theoretical travel time ridge corresponding to $l = 1000$ over-plotted using the white dashed line *(right)*.

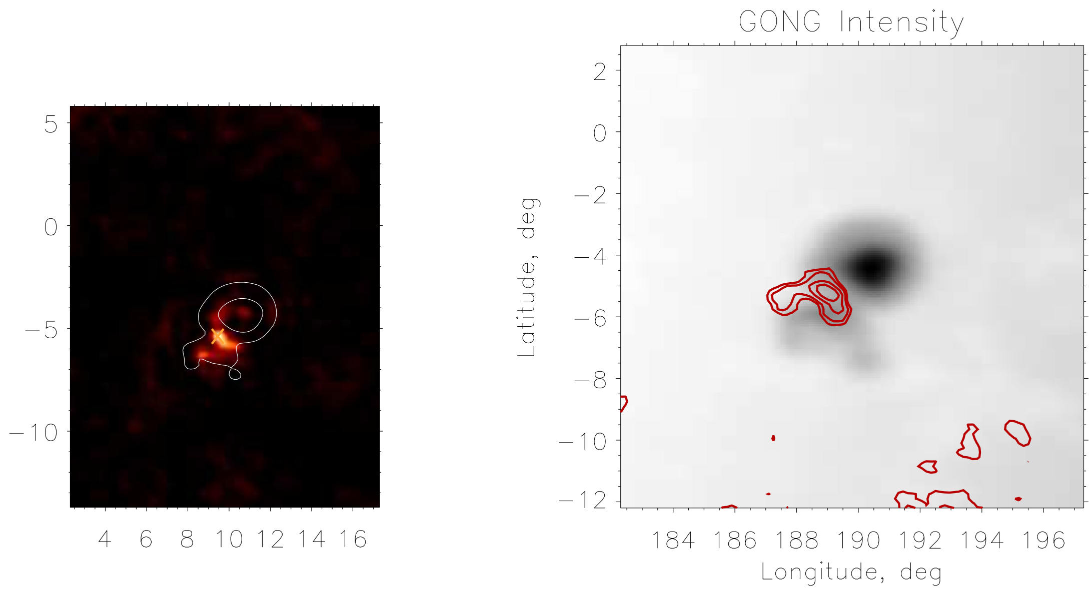

Fig. 11.— *Left:* Egression power snapshot (4-6 mHz) taken around 22:07UT derived from GONG intensity data. Carrington longitude is along the x-axis, latitude is along y-axis. Contours are WL intensity. Location of the time-distance source marked by 'X'. *Right:* Hinode SOT Stokes V image with egression power contours over-plotted in red. GONG intensity contours over-plotted in yellow and time-distance source location marked as 'X'.